JGR Solid Earth

RESEARCH ARTICLE
10.1029/2018JB016928

This article is a companion to Miyazaki and Korenaga (2019), https://doi.org/10.1029/2018JB016932.

Key Points:
- The thermal and chemical evolution of magma ocean is modeled with a self-consistent thermodynamic model
- End-member scenarios are presented with crystal accumulation and/or matrix compaction
- When compaction is efficient, a basal magma ocean can form even when solidification starts from the bottom

Correspondence to:
Y. Miyazaki,
yoshinori.miyazaki@yale.edu

Citation:
Miyazaki, Y., & Korenaga, J. (2019). On the timescale of magma ocean solidification and its chemical consequences: 2. Compositional differentiation under crystal accumulation and matrix compaction. *Journal of Geophysical Research: Solid Earth*, *124*, 3399–3419. https://doi.org/10.1029/2018JB016928

Received 24 OCT 2018
Accepted 13 MAR 2019
Accepted article online 18 MAR 2019
Published online 5 APR 2019

On the Timescale of Magma Ocean Solidification and Its Chemical Consequences: 2. Compositional Differentiation Under Crystal Accumulation and Matrix Compaction

Yoshinori Miyazaki[1] **and Jun Korenaga**[1]

[1]Department of Geology and Geophysics, Yale University, New Haven, CT, USA

Abstract The solidification of a putative magma ocean sets the stage for subsequent subsolidus mantle convection. Whereas it may have resulted in a compositionally stratified mantle, the efficiency of relevant processes to cause chemical differentiation, such as crystal accumulation and matrix compaction, remains uncertain. The purpose of this study is to present the thermochemical structure of end-member cases where potential differentiation mechanisms are taking full effect. We employ a self-consistent thermodynamic model to make our model consistent in both thermal and chemical aspects. The accumulation of crystals at the base of magma ocean can enrich the upper mantle with iron, but such a global-scale compositional stratification is likely to be quickly eliminated by gravitational instability, leaving small-scale heterogeneities only. On the other hand, the compaction of solid matrix in the deep mantle creates a long-lasting molten layer above the core-mantle boundary. Our results suggest that the efficiency of compaction is the key factor to generate compositional stratification during solidification.

1. Introduction

It is widely accepted that terrestrial planets have experienced large-scale mantle melting and that the subsequent solidification of a magma ocean may have created a certain degree of chemical differentiation in the silicate mantle (e.g., Solomatov & Stevenson, 1993a; Abe, 1993, 1997; Elkins-Tanton et al., 2003). Some hypothesize that low seismic velocity anomalies observed in the lowermost mantle of the Earth and isotopic heterogeneities within the convecting mantle may be remnants of such differentiation during the solidification (e.g., Labrosse et al., 2007; Mukhopadhyay, 2012; Brown et al., 2014). Also, the solidification of the magma ocean sets the initial condition for subsolidus mantle convection, thereby being critical for the likelihood of plate tectonics in the early Earth (Korenaga, 2013; Foley et al., 2014). How the putative magma ocean solidified, however, currently suffers from large uncertainties, and its chemical consequences thus remain controversial.

A difficulty in estimating the compositional structure of the postmagma ocean stage lies in our limited understandings of the dynamical behavior of a crystal-melt mixture and element distribution between the two phases under high pressures. Regarding the dynamics, the degree of differentiation is determined by whether crystals are suspended at the base of magma ocean, which is regulated by the competition between crystal settling and entrainment under turbulent convection (Martin & Nokes, 1989; Solomatov et al., 1993). Controlling factors for settling include the mineral assemblage of crystal and its density contrast against the surrounding melt, whereas those for entrainment are crystal radius and the viscosity of melt (Solomatov & Stevenson, 1993b); these factors are largely unconstrained under deep mantle conditions.

In addition to the likelihood of crystal accumulation, the composition of solidifying phases also plays an important role in determining the degree of chemical differentiation. Element partitioning between crystal and melt, however, is still controversial at high pressures; for example, measurements for the partitioning coefficient of iron differ considerably among studies (Andrault et al., 2012; Tateno et al., 2014). This makes magma ocean dynamics more uncertain because the concentration of iron can reverse the density contrast between melt and crystal (Nomura et al., 2011; Elkins-Tanton, 2012). As the iron concentration may vary significantly with pressure, a good thermodynamic model that can estimate melt chemistry is required for the entire mantle pressure range.

The compositional structure of a magma ocean could evolve further even after magma solidifies over the critical melt fraction (typically ~40%) and starts to behave rheologically as solid. The compaction of solid matrix may reduce melt fraction and create further differentiation at the same time, although the percolation of melt through the crystal-melt mixture can be a rate-limiting factor (Solomatov, 2015). This, again, depends on poorly known factors including permeability, crystal radius, and density contrast. Also, the thermal or compositional structure of the rigid layer is likely to be gravitationally unstable, and the Rayleigh-Taylor instability may cause an overturn (Elkins-Tanton et al., 2003; Elkins-Tanton, 2008). The instability, however, may not necessarily result in an overturn if the wavelength of the instability is short compared to the length scale of the mantle (Maurice et al., 2017; Boukaré et al., 2018). The compositional structure after magma ocean solidification is thus a complex problem, yet it is crucial for the subsequent evolution of terrestrial planets.

In this study, therefore, we create a model to predict chemical consequences for different solidification scenarios. Rather than presenting one possible solution, we aim to place bounds on the range of compositional differentiation under plausible dynamical and chemical considerations. Given the current uncertainties on crystal accumulation and matrix compaction, we consider the following four end-member cases: (1) with no crystal accumulation nor matrix compaction, (2) with crystal accumulation only, (3) with matrix compaction only, and (4) with both crystal accumulation and matrix compaction. For all of these cases, we use a self-consistent thermodynamic model, constructed in our companion paper (Miyazaki & Korenaga, 2019), to track the chemical evolution of the system. The use of such a thermodynamic model enables us to have density contrast, element partitioning, and melting temperature internally consistent. The paper is organized as follows. First, the theoretical framework of our parameterized convection model is presented, together with the formulation of crystal accumulation and matrix compaction. After presenting modeling results of four cases, the gravitational stability of resulting structures is discussed. In the last part of the paper, the degree of chemical heterogeneity created by each differentiation mechanism is summarized with a perspective on the thermal evolution of the core.

2. Method

To study the thermochemical evolution of a solidifying magma ocean, we employ a one-dimensional parameterized convection model using the spherical shell geometry. We track the potential temperatures and thicknesses of the following two layers: soft and rigid layers. These layers are defined by their melt fractions, ϕ, by $\phi \geq 0.4$ and $0 \leq \phi < 0.4$, respectively. The value of 0.4 is a typical critical melt fraction for the rheological transition, where the rheology of a crystal-melt mixture transforms from liquid to solid (Campbell & Forgacs, 1990) and has been commonly adopted by previous studies (e.g., Abe, 1993; Solomatov & Stevenson, 1993a; Monteux et al., 2016). At every time step, the compositions of crystal and melt are calculated at 200 discretized grid cells, equally distributed over the entire mantle depth, using Gibbs free energy minimization, and the results of minimization determine the melt fraction thus the thicknesses of soft and rigid layers. Because convective heat flux changes by many orders of magnitude upon the rheological transition, thermal evolution and Gibbs free energy minimization are solved sequentially so that thermal and compositional structures are internally consistent. Equations for thermal evolution and our strategy for tracking chemical evolution are described in sections 2.1 and 2.2, respectively. How we treat crystal accumulation and matrix compaction is described in the subsequent sections.

2.1. Thermal Evolution

The thermal evolution of the ith layer ($i = 1, 2, \dots$) is determined by the following heat balance equation:

$$C_i(t)\frac{\mathrm{d}T_i}{\mathrm{d}t} = Q_{i-1}(t) - Q_i(t), \tag{1}$$

where T_i denotes the potential temperature, C_i is the heat capacity, Q_i is convective heat loss to the layer above or to the surface, and t is time. Layers are labeled from the bottom, that is, $i = 1$ corresponds to the lowermost layer above the core-mantle boundary. Heating from the layer beneath is equal to convective heat loss at the underlying layer (i.e., $(i-1)$th layer), and Q_0 indicates heating from the core. The heat flow Q_i is calculated as $4\pi r_i^2 F_z$, where r_i is the radius of the top boundary of the ith layer, and F_z is convective heat flux. In the soft layer, where magma behaves as liquid, the convective heat flux is expressed as (Siggia, 1994; Solomatov, 2015)

$$F_z = 0.089\frac{k_c(T_m - T_s)}{L}Ra^{1/3}, \tag{2}$$

where T_m, L, and Ra denote the potential temperature, the thickness, and the Rayleigh number of the layer, respectively, T_s is surface temperature, and k_c is thermal conductivity, for which we adopt a value of 2 $W \cdot m^{-1} \cdot K^{-1}$ (Lesher & Spera, 2015). The effect of viscosity is incorporated in the Rayleigh number, which is given by

$$Ra = \frac{\alpha \rho_0^2 C_p g (T_m - T_s) L^3}{k_c \eta}, \tag{3}$$

where α denotes thermal expansivity, ρ is density, C_p is heat capacity per unit mass, g is gravity, and η is viscosity. Because liquid viscosity is known to have a much weaker temperature dependency compared to solid (Liebske et al., 2005), we assume a constant viscosity of 10 Pa s at all pressures and temperatures (Dingwell et al., 2004). All thermodynamic parameters, including thermal expansivity, density, and heat capacity, are obtained from the Gibbs free energy (section 2.2). The heat capacity of a layer C_i is obtained by adding the heat capacity of constituting grids, and α, ρ, and C_p in equation (3) are calculated based on the Gibbs free energy of the uppermost grid. Convective heat transport can be affected by turbulence when the Rayleigh number is sufficiently high (Siggia, 1994; Solomatov, 2015). Equation (2) may overestimate the heat flux by a factor of 20 at most when the Rayleigh number is the highest at the beginning, although the difference decreases with time. The timescale of our evolution becomes longer by an order of magnitude if we adopt a scaling law describing turbulent convection. The effect of cooling timescale on the compositional structure is discussed in section 4.3.

The convective heat flux of the rigid layer ($0 \leq \phi < 0.4$) can be parameterized similarly, but it is significantly smaller than that of the soft layer because of high viscosity. Whereas the viscosity of liquid is 0.1–100 Pa s, that of solid is considered to be larger than 10^{18} Pa s (e.g., Karato & Wu, 1993), reducing heat flux by 10^6. Because our focus is on the evolution until the transition to subsolidus convection, neglecting such small convective heat flux does not affect the overall thermal evolution for the period under consideration. Heating from the layer beneath (Q_{i-1}) is therefore ignored. Note that a soft layer ($\phi > 0.4$) can emerge below a rigid layer in some scenarios. The convective heat flux out of such an internal soft layer would be zero, because it is practically insulated by the overlying rigid layer.

When the lowermost layer is the soft layer, the core heat flux Q_0 is calculated as

$$Q_0 = 4\pi r_c^2 \frac{k_c (T_{\mathrm{core}} - T_b)}{D}, \tag{4}$$

where r_c is the core radius, T_{core} and T_b are the potential temperatures of the core and the lowermost layer of the system, respectively, and D is the thickness of the bottom boundary layer, which is determined from the local stability criterion (Stevenson et al., 1983). Because of its high viscosity, the thickness of the boundary layer is expected to be much thicker for the rigid layer than for the soft layer, and therefore, the core heat flux is neglected, that is, $Q_0 = 0$, when the lowermost layer becomes rigid. The thermal evolution of the core is described as

$$C_{p,\mathrm{core}} \frac{\mathrm{d}T_{\mathrm{core}}}{\mathrm{d}t} = -Q_0, \tag{5}$$

where $C_{p,\mathrm{core}}$ is the heat capacity of the core, for which the value of 1.5×10^{27} J K^{-1} is employed (Buffett et al., 1996). The potential temperature of the core is initially assumed to be 6000 K.

The surface temperature T_s is determined by the greenhouse effect of atmosphere. Degassing of H_2O and CO_2 from magma ocean is predicted to create an atmosphere as thick as 100 bar (Abe & Matsui, 1988; Elkins-Tanton, 2008), and its blanketing effect may have maintained the surface molten for as long as a few million years (Matsui & Abe, 1986; Hamano et al., 2013). We assume a constant temperature of 1500 K for T_s in this study.

2.2. Gibbs Free Energy Minimization

The melt and crystal compositions of each grid are calculated using Gibbs free energy minimization, the implementation of which is described in Miyazaki and Korenaga (2017). For crystal compositions, olivine and orthopyroxene are considered at upper-mantle pressures, whereas bridgmanite and ferropericlase are

at lower-mantle pressures. We use the thermodynamic database of Stixrude and Lithgow-Bertelloni (2011) for solid components and that constructed in our companion paper (Miyazaki & Korenaga, 2019) for liquid components (see their Table 2, the n=1 case without the experiment on chondritic primitive mantle). Because the liquid database is constructed based on high-pressure melting experiments, melting temperatures in the upper-mantle pressure are not accurately represented. Our focus is on the solidification of the lower mantle, and therefore this limitation has only a minor impact on our results and discussion. We adopt a simple MgO-FeO-SiO_2 ternary system (e.g., Boukaré et al., 2015), and the initial magma ocean is assumed to be compositionally homogeneous. The initial composition has an Mg number of 0.895, and it imitates the composition of pyrolite (McDonough & Sun, 1995; Lyubetskaya & Korenaga, 2007), with the ternary composition of MgO: 42.2 wt%, FeO: 8.7 wt%, and SiO_2: 49.1 wt%. The existence of other oxides including Al_2O_3 and CaO is likely to affect the melting temperature of mantle materials, although more studies are needed to better understand the melting of such oxides (Fiquet et al., 2010; Andrault et al., 2017; Braithwaite & Stixrude, 2019). Results of Monte Carlo inversion in our companion paper (Miyazaki & Korenaga, 2019) suggest that the nonideality of the mixing becomes negligible when the concentration of an oxide is low enough.

The temperature of each grid is calculated from the potential temperature of the corresponding layer when the layer is under liquid state convection. Under vigorous convection, the temperature is assumed to change adiabatically as follows

$$\frac{\mathrm{d}T}{\mathrm{d}P} = \frac{\alpha T}{\rho C_p}, \tag{6}$$

where P denotes pressure. Thermal expansivity and heat capacity are obtained by differentiating the Gibbs free energy of each grid, according to fundamental thermodynamic relations. By doing so, the effect of phase change is included self-consistently when calculating material properties at temperatures between the solidus and the liquidus. Once the convective heat flux of the layer becomes negligible, however, cooling ceases, and each grid maintains the last temperature when convection was operating.

2.3. Crystal Accumulation

When the possibility of crystal accumulation is considered, we assume that all newly formed grains in the entire soft layer will stack at the base of the layer if grains are heavier than the coexisting liquid. Gibbs free energy minimization assumes chemical equilibrium between melt and crystal at each depth level, and liquid state convection mixes both crystal and melt thoroughly. During such convective mixing, the composition of crystal is unlikely to be modified because the timescale of Mg-Fe interdiffusion (Buening & Buseck, 1973) is much longer than a convective timescale. We therefore use the average compositions of crystal and melt within the soft layer and calculate their densities under the pressure and temperature condition at the bottom of the soft layer. Because the compaction of crystal-melt mixture can take place only slowly, a pile of crystals at the base will include a certain amount of liquid so that the melt fraction of the pile becomes equal to the critical melt fraction. The liquid trapped in the mixture is subtracted from the remaining magma. We conduct Gibbs free energy minimization for a newly formed accumulated layer so that the layer is in chemical equilibrium.

2.4. Matrix Compaction

The matrix of the rigid layer experiences compaction owing to density difference between melt and crystal. The compaction timescale may be estimated by $\eta_s/(\rho_s - \rho_l)gL$, where η_s is the viscosity of solid matrix, ρ_s and ρ_l are the densities of solid and melt, respectively, and L is the thickness of the rigid layer. This gives a timescale shorter than 100 years for $L \sim$100 km with densities and viscosity employed in this study, but it is known that compaction is limited by percolation (Reese & Solomatov, 2006). The percolation velocity of melt, v_{perc}, is described as

$$v_{\mathrm{perc}} = \frac{1}{\phi}\frac{k_m}{\eta_l}(\rho_s - \rho_l)g, \tag{7}$$

where k_m is the permeability of solid matrix, and η_l is the viscosity of melt. In our model, compaction is modeled by transporting $\phi v_{\mathrm{perc}}\Delta t$ of melt at each grid. When $v_{\mathrm{perc}} > 0$, for example, melt is transported upward, and in exchange, the same amount of solid is transported downward from the overlying grid. Heat transport associated with compaction is described by assigning the weighted average of potential temperatures of transported and original materials as the new potential temperature. To ensure chemical equilibrium between the transported melt and the surrounding, Gibbs free energy minimization is performed at each time step.

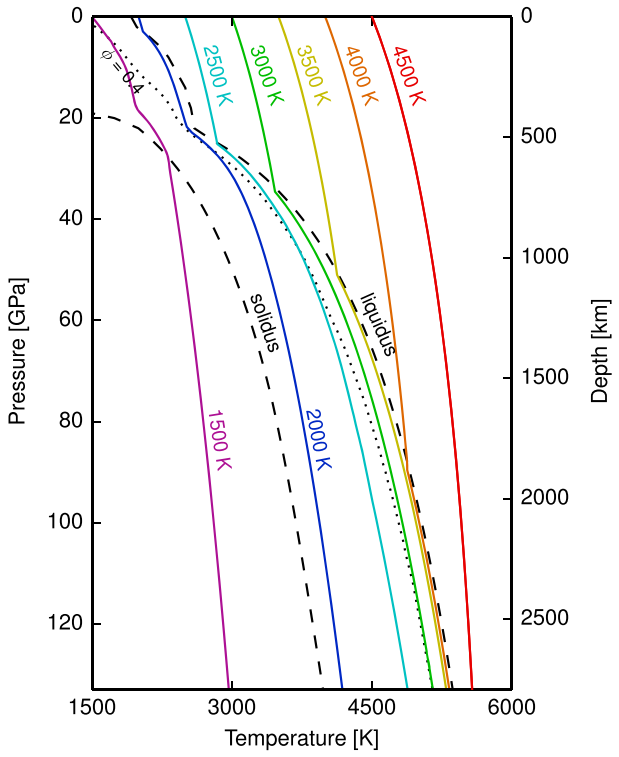

Figure 1. Adiabatic temperature profiles with potential temperatures of 1500 K (purple), 2000 K (blue), 2500 K (cyan), 3000 K (green), 3500 K (yellow), 4000 K (orange), and 4500 K (red) for pyrolitic composition. The solidus and liquidus of pyrolite (dashed), along with temperature where melt fraction is 40% (dotted), are also shown for comparison.

Permeability is given as a function of grain size, d, and melt fraction (Dullien, 1992):

$$k_m = \frac{d^2}{150}\frac{\phi^3}{(1-\phi)^3}. \quad (8)$$

Because percolation velocity is a linear function of permeability, percolation becomes quickly inefficient as melt fraction decreases. The degree of percolation also depends strongly on grain size, but the value of expected grain size in magma ocean is not well constrained (Solomatov & Stevenson, 1993c). We therefore test two grain sizes, 1 mm and 1 cm, to model the compaction, which corresponds to a change in percolation flux by 2 orders of magnitude.

3. Results

To facilitate the discussion of our modeling results, adiabats with different potential temperatures are first presented in Figure 1. An adiabatic temperature profile can be assumed for convecting layers with liquid viscosity. The other layers do not have to follow an adiabatic temperature profile because the timescale for solid state convection is much longer than the duration we consider, as noted in section 2. The adiabat increases smoothly with pressure when the system is completely molten, but the adiabat gradient changes discontinuously when crystals start to precipitate. This is because thermal expansivity and heat capacity both increase due to phase change. The magnitude of increase is larger for thermal expansivity than heat capacity, so the adiabat of partially molten materials becomes steeper than that of pure solid or liquid. Such an effect is strongest near the liquidus because Mg-bridgmanite rapidly melts as temperature approaches the liquidus with our thermodynamic model.

All the cases considered start with an adiabatic temperature profile with the potential temperature of 4400 K, so that the whole system is initially above the liquidus. The choice of this initial condition is motivated partly by its simplicity, though it appears to be reasonable according to some recent numerical studies of moon-forming giant impact (e.g., Canup, 2008; Nakajima & Stevenson, 2015). Because the surface temperature is set to 1500 K, the surface remains molten during the entire model run. With the thermodynamic databases adopted in this study, the transition from a soft layer to a rigid one occurs from the base of magma ocean, and the thickness of the rigid layer grows with time. The soft layer near the surface cools down rapidly through vigorous convection because of low viscosity; other layers with solid viscosity convect only sluggishly, and thus convective cooling in those layers is ignored. Each model run is continued until the potential temperature of the surface soft layer reaches 1540 K. The potential temperature continues to approach 1500 K, but the thickness of the molten layer at the surface remains mostly unchanged during subsequent evolution, so we define this state as a final thermal structure.

3.1. Without Crystal Accumulation nor Matrix Compaction (Equilibrium Crystallization)

In the simplest case with no crystal accumulation nor matrix compaction, composition is not altered by any process, so the entire system retains a homogeneous pyrolitic composition. The melt fraction starts to decrease from the lowermost mantle until it reaches 40%, and the thickness of a rigid layer grows with time. As advective heat loss from the rigid layer is assumed to be negligible, the temperature of grids in the rigid layer remains constant. The final thermal structure is equivalent to the 40% melting temperature of pyrolite (Figure 2), which is closer to the liquidus than the solidus. The reason for this high 40% melting temperature can be traced back to the experiments of Du and Lee (2014) and Deng and Lee (2017), which are employed to determine our thermodynamic model; these experiments show the same trend for the MgO-FeO binary system.

With a constant liquid viscosity of 10 Pa s, the melt fraction of the entire lower mantle falls below 40% in the first 5,000 years, and the rigid layer covers most of the mantle within 7,000 years except for the molten layer at the surface. This timescale is proportional to $\eta^{1/3}$ as seen in equations (2) and (3). This is on the same

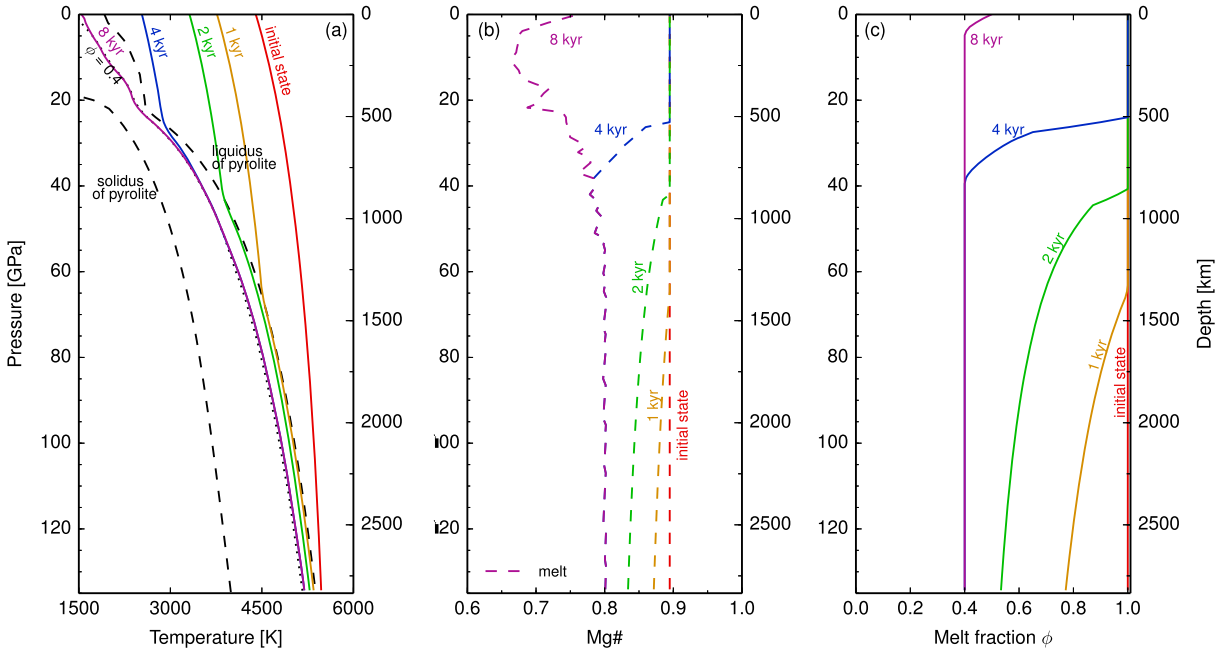

Figure 2. Thermal evolution of magma ocean with no crystal accumulation nor matrix compaction. The profiles of (a) temperature, (b) the Mg# of melt, and (c) melt fraction at 0 kyr (red), 1 kyr (orange), 2 kyr (green), 4 kyr (blue), and 8 kyr (purple) are shown. The final thermal structure is equivalent to the 40% melting temperature of pyrolite (dotted). The potential temperature of the surface soft layer reaches 1540 K at 8 kyr, and thermal structure remains mostly unchanged during subsequent evolution. In (a), the solidus and liquidus temperatures of pyrolite are also shown (dashed).

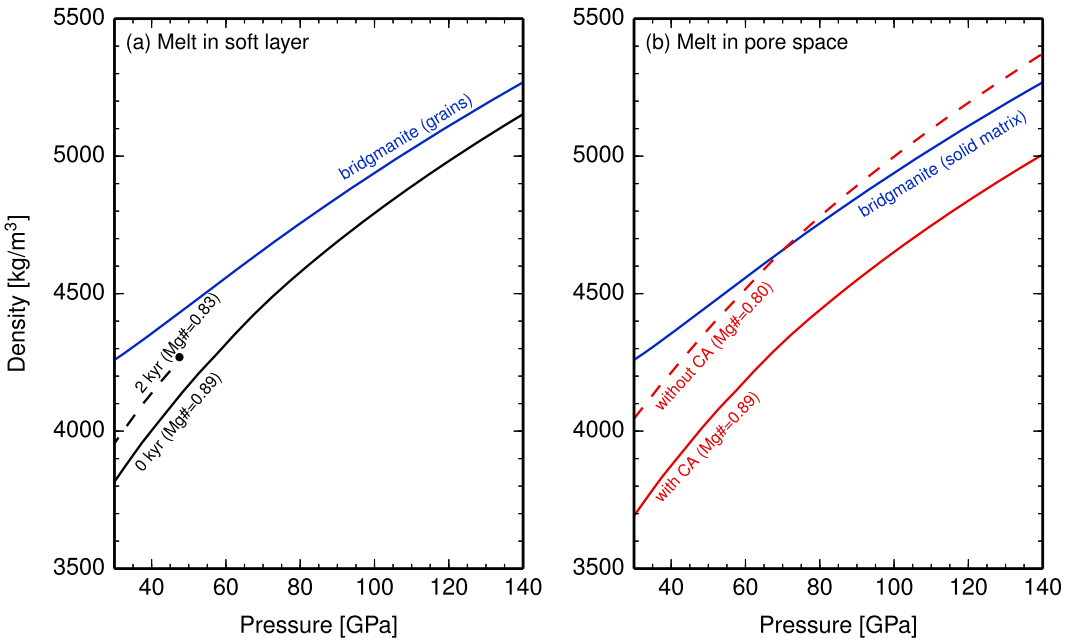

Figure 3. Density profiles of melt and crystal forming during the evolution along the liquidus temperature of undifferentiated magma ocean. (a) Densities of melt in the soft layer at 0 kyr (black solid) and 2 kyr (dashed) and bridgmanite fractionating at the liquidus (blue). For 2 kyr, the profile only within the soft layer is shown. Bridgmanite is denser than the melt throughout the evolution. (b) Densities of melt in pore space (red) and solid matrix (blue) within the rigid layer. The melt includes less iron for the case with crystal accumulation (CA, solid) with Mg# of 0.89, whereas it is more enriched in iron for the case without CA (dashed). Solid matrix is mostly composed of Mg-bridgmanite for both cases. Density crossover takes place for the case without CA.

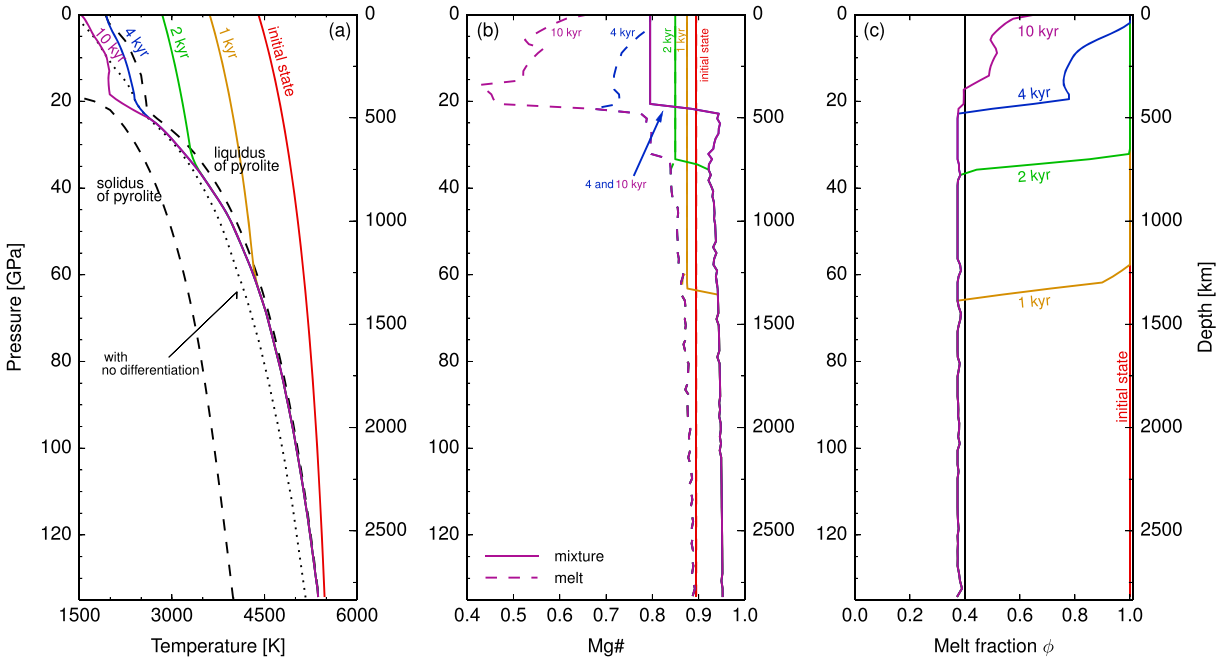

Figure 4. Thermal evolution of magma ocean when crystals accumulate at the base of magma ocean. Matrix compaction is not considered. The profiles of (a) temperature, (b) Mg#, and (c) melt fraction at 0 kyr (red), 1 kyr (orange), 2 kyr (green), 4 kyr (blue), and 10 kyr (purple) are shown. The potential temperature of the surface soft layer reaches 1540 K at 10 kyr, after which thermal structure remains mostly unchanged. Because the system experiences compositional differentiation, shallower region becomes enriched in iron. In (a), the final thermal structure for the case without crystal accumulation is also shown for comparison (dotted), together with the solidus and liquidus temperatures of pyrolite (dashed).

order with the estimate by Monteux et al. (2016), which predicted the duration of 15,000 years from the start of solidification at the core-mantle boundary to the rheological transformation at the surface, using liquid viscosity of 100 Pa s. As cooling proceeds, the difference between the surface and potential temperatures becomes smaller, and the soft surface layer thins gradually, resulting in slower cooling.

The stability of resulting thermal structure can be evaluated by comparing with the adiabatic gradient. The fact that the 40% melting temperature is reached first at the bottom and the rigid layer grows upward indicates that the gradient of 40% melting temperature is steeper than the adiabatic gradient. The final thermal structure is thus superadiabatic, and the Rayleigh-Taylor instability can operate (see section 4.1 for further discussion).

3.2. With Crystal Accumulation Only

When grain size in magma ocean is larger than 10^{-3} to 10^{-2} m, convective entrainment becomes inefficient, and crystal accumulation proceeds at the base of a soft layer (Solomatov & Stevenson, 1993b), creating compositional differentiation. Because iron is preferentially partitioned to the melt phase, grains have higher Mg# than the remaining liquid when grains start to fractionate near the base of magma ocean. Despite their high Mg#, newly formed grains are denser than the remaining liquid (Figure 3a), and therefore the accumulated pile enriched in MgO forms at the base of magma ocean (Figure 4b). Through this process, the remaining magma ocean becomes more enriched in iron, but grains composed of bridgmanite remain denser throughout the solidification of the lower mantle. We note that the experimentally determined Fe-Mg partition coefficient also suggests the enrichment of iron in the melt phase for all lower-mantle pressures (Nomura et al., 2011). Crystal accumulation will continue to create a Mg-rich layer, and when the accumulated pile covers the entire lower mantle, the Mg# of the remaining magma ocean (i.e., the soft layer) falls below 0.8 (4 kyr in Figure 4).

Because the melting temperature of MgO is higher than that of FeO, the accumulated pile with high Mg# reaches 40% melt fraction at higher temperatures than unfractionated pyrolite (Figure 4a). The accumulated pile therefore immediately transforms into a rigid layer although the temperature at the point of accumulation is higher than the 40% melting temperature of pyrolite, and the temperature at the point of accumulation is maintained during the subsequent evolution. In our implementation, we gather all grains in the soft layer

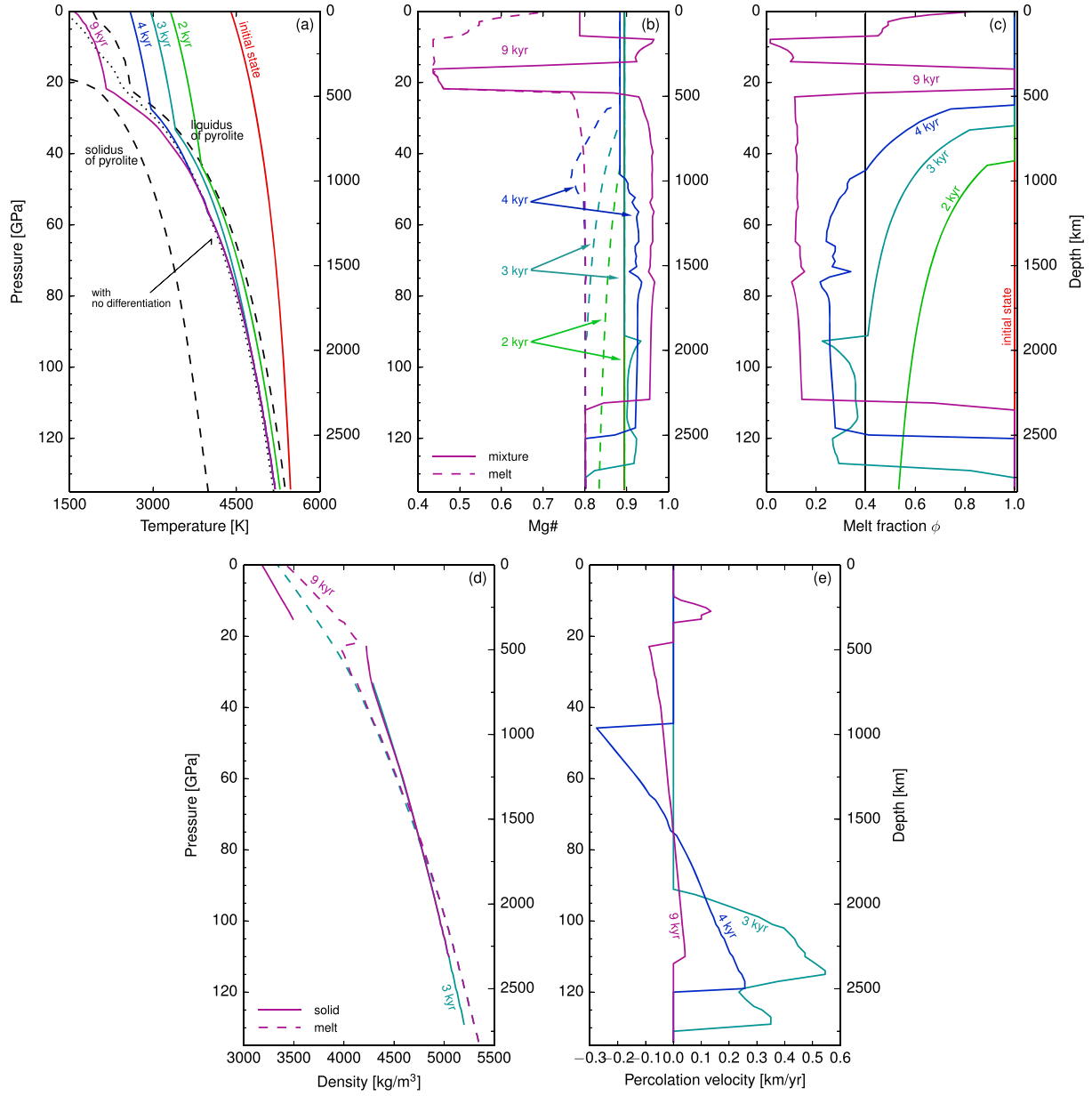

Figure 5. Thermal evolution of magma ocean when the rigid layer experiences matrix compaction. The accumulation of newly formed grains at the base is not considered here. The profiles of (a) temperature, (b) Mg#, (c) melt fraction, (d) density, and (e) percolation velocity are shown. Each color indicates 0 kyr (red), 2 kyr (green), 3 kyr (blue-green), 4 kyr (blue), and 9 kyr (purple). The potential temperature of the surface soft layer reaches 1540 K at 9 kyr, after which thermal structure remains mostly unchanged. Percolation becomes slow when melt fraction reaches ∼0.2, and matrix compaction practically ceases after 9 kyr. In (a), the final thermal structure for the case without crystal accumulation nor matrix compaction is also shown for comparison (dotted), together with the solidus and liquidus temperatures of pyrolite (dashed).

with some amount of melt so that the melt fraction of the accumulated pile becomes 40%, but after Gibbs free energy minimization, the melt fraction in some region slightly decreases below the critical value (Figure 4c).

With more iron contained in the shrinking soft layer, temperature lower than the 40% melting temperature of pyrolite is necessary for the layer to become rigid. The concentration of iron in the soft layer continues to increase until grains become lighter than the iron-rich liquid, which happens soon after 4 kyr. At the end of the evolution (10 kyr), the surface region up to 20 GPa retains a homogeneous composition with an Mg# of 0.8, and the temperature of the upper mantle is lower by ∼300 K compared to the case without differentiation. The final thermal structure becomes steeper than the case without crystal accumulation, which is likely to reduce the timescale of the Rayleigh-Taylor instability (see section 4.1 for further discussion).

3.3. With Matrix Compaction Only

Because density difference between solid matrix and melt in pore space always exists, the rigid layer inevitably experiences some degree of compaction. The process is, however, rate-limited by percolation, and our results indicate that compaction is inefficient when a grain size of 1 mm is assumed. In such case, percolation velocity is ~1 m~year^{-1}, and its effect is insignificant within the duration of our model run. The result with a grain size of 1 mm is virtually identical to the case without matrix compaction. With a larger grain size of 1 cm, however, permeability increases by 2 orders of magnitude, and a noticeable impact is observed.

The direction of melt extraction is controlled by density difference between solid matrix and melt in pore space. When melt is lighter than solid matrix, melt is extracted and transported upward. For the case without crystal accumulation, however, the density contrast is reversed in the deep mantle, and the melt migrates toward the core-mantle boundary. Such density crossover is observed at around ~75 GPa (Figures 3b and 5d). This happens to coincide with the depth that the spin crossover of iron occurs, below which iron is suggested to be strongly enriched in the melt phase (Nomura et al., 2011). Our model also predicts that melt is heavier than solid matrix throughout the entire upper mantle, but the melt is lighter near the surface in the actual Earth. Density at the upper mantle may not be accurately described because our thermodynamic model is based on melting experiments at lower mantle conditions. Melt accumulating at the 660-km discontinuity is likely to be transported to the surface in reality, but this does not affect our prediction on the solidification process of the lower mantle.

Melt extracted from depth below 75 GPa is transported to the core-mantle boundary, and it forms a completely molten layer with a thickness of 500 km. Melt in the shallower part of the lower mantle and that in the upper mantle are both delivered to the 660-km discontinuity and create another molten layer. Because the melt in pore space is enriched in iron compared to the solid matrix, these layers have low Mg# compared to the initial. The melt layer above the core-mantle boundary has the Mg# of 0.8, whereas that at the 660 km may have Mg# as low as 0.45. The compacted solid matrix, on the other hand, becomes depleted in iron (Figure 5b). The upward transport of iron-rich melt alters the composition of the soft layer. As the layer becomes enriched in iron, its melting temperature goes down, which results in a colder final thermal structure compared to the case without matrix compaction (Figure 5a).

Because the difference in density between melt and solid and thus percolation velocity increases nearly linearly with depth, the net amount of melt extraction is roughly the same regardless of depth. The melt fraction in the rigid layer therefore decreases almost uniformly with depth (Figure 5c). Because percolation velocity is a function of the cube of melt fraction, melt extraction becomes quickly inefficient. When melt fraction reaches $\phi \sim 0.2$, matrix compaction practically ceases. Although scaling analysis predicts that percolation length scale will be as short as ~100 km for grain size of 1 cm (Reese & Solomatov, 2006), a large-scale compaction can create a basal magma ocean with a thickness of ~500 km within 10 kyr. Further compaction can potentially occur if dihedral angle is small enough, where pore fluid becomes interconnected even with low melt fraction. In such case, the midmantle may compact until the region is almost completely depleted of melt, resulting in a midmantle with higher Mg# than predicted in Figure 5b.

3.4. With Crystal Accumulation and Matrix Compaction

For the rigid layer created by crystal accumulation, melt moves upward as opposed to the case without the accumulation. The Mg# of melt in the pore space is higher (~0.89; Figure 4b), so the melt is lighter than the solid matrix for the entire lower mantle (Figure 3b). Compared to the rigid layer considered in the previous section, the accumulated pile has 10% larger Mg#, and the melt in pore space in equilibrium with solid matrix also contains more MgO (Figure 6b). Because of the low Fe-Mg partition coefficient, additional iron in the bulk system is mostly partitioned into the melt phase, resulting in a larger density contrast.

As in the case without crystal accumulation, melt in the pore space is enriched in iron compared to the initial. When the iron-rich melt is extracted and transported upward, this process decreases the Mg# of the soft layer, resulting in lower melting temperature and higher density. The combined effects of crystal accumulation and matrix compaction can rapidly raise the Mg# of the accumulated pile above 0.95, which is the highest among the four cases considered in this study. When the accumulated pile grows up to the pressure of 50 GPa at 2 kyr, however, grains accumulating at the base of the soft layer does not turn into a rheologically rigid pile. The extracted melt from pore space enriches the soft layer with iron, and as a result, the accumulated layer, which is initially the mixture of 60% Mg-rich grains and 40% iron-rich melt, contains enough iron to increase the melt fraction after chemical equilibrium is reached. Between 2 and 3 kyr, the

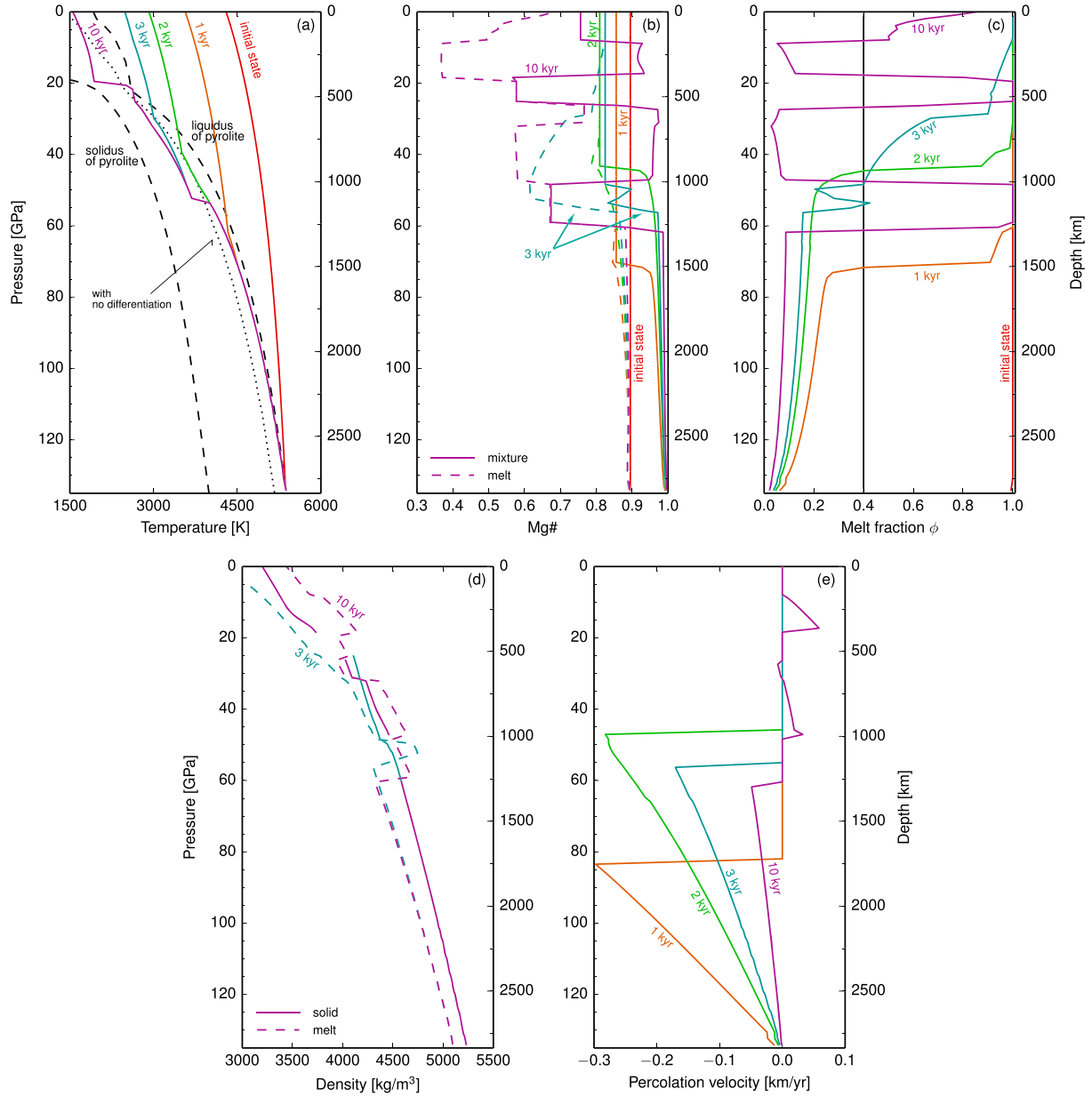

Figure 6. Same as Figure 5 but for the case with both crystal accumulation and matrix compaction. The profiles of at 0 kyr (red), 1 kyr (orange), 2 kyr (green), 3 kyr (cyan), and 10 kyr (purple) are shown. The potential temperature of the surface soft layer reaches 1540 K at 10 kyr, after which thermal structure remains mostly unchanged, and percolation practically ceases.

rigid layer therefore shrinks by compaction instead, and a temperature jump is created because the soft layer continues to cool.

After 3 kyr, the iron-rich soft layer becomes cold enough to turn into a rigid layer, and the formation of rigid layer resumes. Because of low temperature, iron is partitioned more into the melt phase, resulting in Mg# lower than 0.7, and melt becomes heavier than solid matrix. Melt is therefore transported downward, creating a molten layer at ~50 GPa. Such a molten layer is also observed in ~20 GPa, because melt is heavier than solid in the upper mantle in our model. The molten layer in the middle of the lower mantle is inevitable when both crystal accumulation and matrix compaction are operating, resulting in chemical heterogeneity and temperature jump within the lower mantle.

The pure melt layers at midmantle depths are created by the extracted melt from the layers above and below. The mixture of melt from both layers is initially stable, but as melt from the overlying layer dominates,

the melt layer becomes heavier than the underlying solidified layer (Figure 6d). The melt from the layer above is more enriched in iron (Figure 6b) because the Mg# of the soft layer decreases with time as the iron-rich extracted melt is added by the compaction of the rigid layer. Although we did not explicitly model the evolution of such gravitationally unstable melt layers, the iron-rich layers are likely to be transported toward the core-mantle boundary. The consequence of downward transport is discussed in section 4.2.

4. Discussion

4.1. The Rayleigh-Taylor Instability

The final thermal structure after the rheological transition is superadiabatic for all cases, and it is thus gravitationally unstable. Further evolution is likely to be caused by some kind of instability, including solid state convection, porous convection, or the Rayleigh-Taylor instability. The timescale of solid state convection is, however, as large as 1 Myr even for a solid viscosity of 10^{15} Pa s (Solomatov, 2015), and porous convection is rate-limited by slow percolation. The percolation velocity v_{perc} by porous convection is described as

$$v_{\mathrm{perc}} = \frac{1}{\phi}\frac{k_m}{\eta_l}\frac{\alpha\rho\Delta T}{L}g, \tag{9}$$

where ΔT is the difference in potential temperatures between the top and bottom of the considering layer, and L is the thickness of the layer. With the optimistic estimates of grain size (∼1 cm) and potential temperature difference (∼2000 K), the velocity is still smaller than 10^{-3} m∼year^{-1}. The timescale of the Rayleigh-Taylor instability, t_{RT}, on the other hand, can be shorter than the duration of our model runs. The timescale may be expressed as (Turcotte & Schubert, 2002)

$$t_{\mathrm{RT}} = \frac{26\eta_s}{\Delta\rho g L}, \tag{10}$$

where $\Delta\rho$ denotes the difference in potential densities between the top and bottom of the unstable layer. With η_s=10^{15} Pa s, the timescale can be as short as a year.

By using the propagator matrix method of Mondal and Korenaga (2018a), the time and length scales of the Rayleigh-Taylor instability can be investigated in more detail. The propagator matrix method allows us to obtain the dispersion relationship of the Rayleigh-Taylor instability when density and viscosity are given as a function of depth. We first estimate the viscosity of the mantle because the timescale depends linearly on solid viscosity. Our estimate is based on the viscosity profile of the current mantle, $\eta_s(T_{\mathrm{ad}})$, which is assumed as a constant of 10^{19} Pa s in the upper mantle and increases log-linearly from 10^{20} Pa s at the 660-km discontinuity to 10^{22} Pa s at the core-mantle boundary (Figure 7). Viscosity along the solidus, $\eta_s(T_{\mathrm{sol}})$, is then calculated by including a temperature effect assuming an activation energy of $E = 300$ kJ mol^{-1}:

$$\eta_s(T_{\mathrm{sol}}) = \eta_s(T_{\mathrm{ad}})\exp\left(\frac{E}{RT_{\mathrm{sol}}} - \frac{E}{RT_{\mathrm{ad}}}\right), \tag{11}$$

where T_{sol} denotes the solidus of pyrolite calculated using the Gibbs free energy minimization, and T_{ad} is the temperature profile of the current mantle, for which we assume an adiabat with a potential temperature of 1350 °C. Because the melting temperature in the upper mantle is not calculated accurately with our thermodynamic model, the solidus in the upper mantle is taken from Solomatov and Stevenson (1993a). The viscosity of solid matrix can be further reduced with the presence of melt and is parameterized as a function of melt fraction as (Mei et al., 2002)

$$\eta = \eta_s(T_{\mathrm{sol}})\exp(-26\phi). \tag{12}$$

At the critical melt fraction of $\phi \sim 0.4$, viscosity can be as low as 2×10^{13} Pa s. The effect of melt, however, may be overestimated because the experiment of Mei et al. (2002) was conducted only up to the melt fraction of 0.1.

We use potential density to compare densities at two different pressures. Materials are moved along adiabatic paths calculated using equation (6) and Gibbs free energy minimization, so the effect of phase change is automatically included. The reference pressure is chosen at the core-mantle boundary. Here, we consider the consequences of the Rayleigh-Taylor instability for the final structure calculated in section 3. For the cases with matrix compaction (sections 3.3 and 3.4), a pure melt layer is likely to form, and the instability timescale for such melt layer is very different. The fate of such a melt layer is discussed in section 4.2.

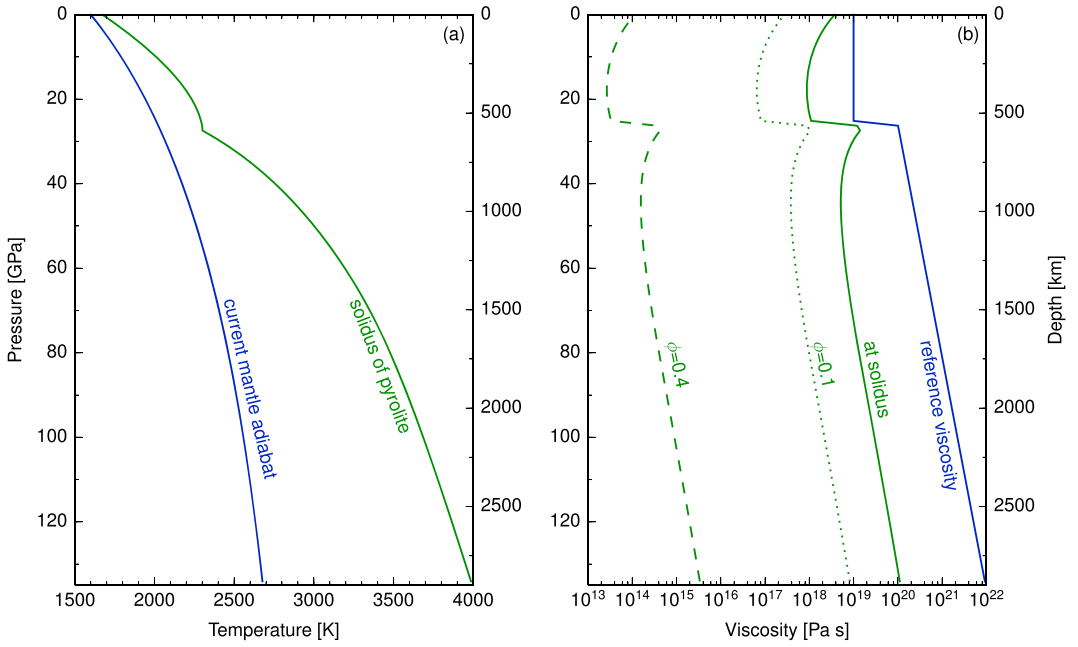

Figure 7. (a) The temperature profile of the current mantle (blue) and the solidus of pyrolite (green). The current mantle is assumed to be adiabatic with a potential temperature of 1350 °C. (b) The estimated viscosity profile (green) at the solidus (solid), with 10% melt (dotted), and with 40% melt (dashed) together with the reference viscosity profile assumed for the current mantle (blue).

4.1.1. Without Crystal Accumulation nor Matrix Compaction (Equilibrium Crystallization)

For the case without any differentiation process (section 3.1), potential density slowly increases upward in the lower half of the mantle (Figure 8a), because the adiabatic gradient of a crystal-melt mixture is very close to the gradient of the final thermal structure, which is the 40% melting curve of pyrolite (Figure 2). During the solidification of the deep region, the timescale for the Rayleigh-Taylor instability decreases only slowly with the thickening of the rigid layer. If a viscosity profile followed the estimate with 40% melt, the timescale for the instability is on the order of 10–100 years during the solidification of the lower mantle. The structure becomes increasingly superadiabatic above 40 GPa, and combined with viscosity reduction at the 660-km discontinuity, the timescale for the instability can drop significantly (Figure 8b), which can be as short as a month. Although the surface temperature is maintained at 1500 K in our study, the final temperature profile is mostly equivalent to the 40% melting temperature of pyrolite, so the final thermal structure will remain the same even when a lower surface temperature is employed.

Because of the short timescale, the operation of the Rayleigh-Taylor instability may quickly change the thermal structure of the rigid layer into an adiabatic one, and the entire magma ocean can quickly cool down to a potential temperature of the surface temperature. The efficiency of cooling, however, is also controlled by the wavelength of the instability. The short wavelength may promote small-scale mixing and prohibit an efficient transport of cold materials at the surface to the deep mantle. A future study is warranted to estimate the degree of cooling by the Rayleigh-Taylor instability.

4.1.2. With Crystal Accumulation Only

A similar trend can be observed for the case with crystal accumulation only, although a timescale is always shorter than the case with equilibrium crystallization. This is because density difference is larger due to compositional differentiation. For the case with crystal accumulation only, potential density in the upper mantle remains constant because the layer remains homogeneous. When the soft layer is enriched in iron at the final stage of evolution, newly formed Mg-rich crystals become lighter than the melt, meaning that the accumulated pile will not be created. Because crystal settling will not occur in such case, the surface melt layer is expected to gradually cool down and solidify without any compositional differentiation. It has been argued that the last iron-rich remnant created by fractional solidification may be extremely heavy, and the remnant could directly be transported to the core-mantle boundary as the result of the Rayleigh-Taylor insta-

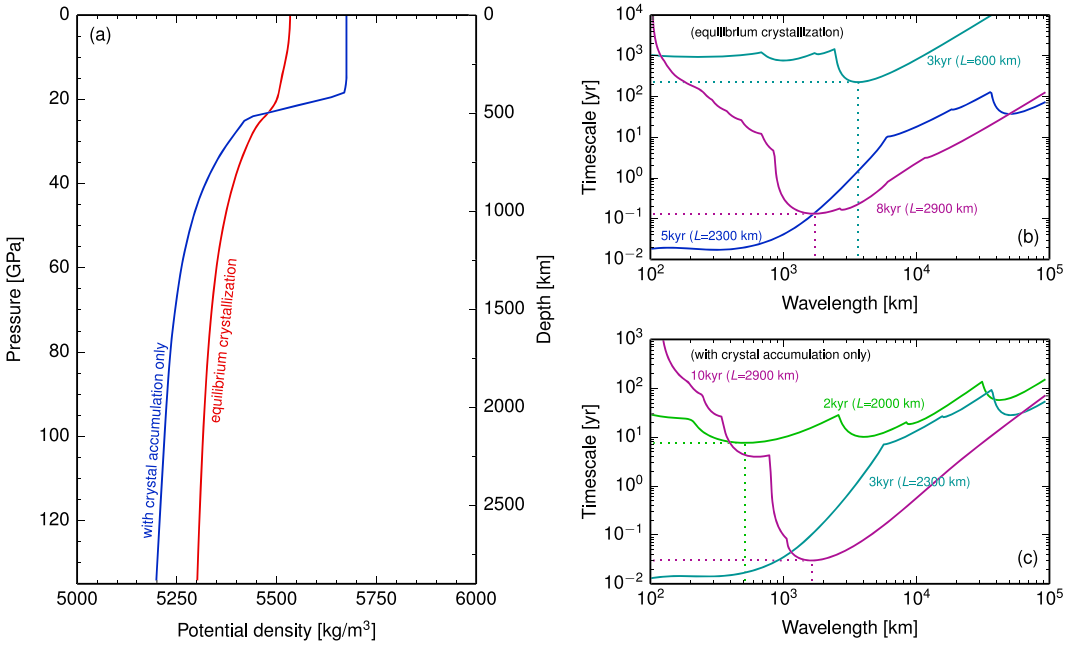

Figure 8. (a) Potential density profile of the final structure, and (b, c) dispersion relationship for the Rayleigh-Taylor instability obtained by the propagator matrix method. Cases with equilibrium crystallization (red in (a) and panel (b)) and with crystal accumulation only (blue in (a) and panel (c)) are shown. In (b) and (c), color indicates 2 kyr (green), 3 kyr (blue-green), 5 kyr (blue), and final stage (purple). Dotted lines denote the timescales and wavelengths of the most unstable perturbations. The thickness of the rigid layer L is also shown in parentheses.

bility (Ballmer et al., 2017; Maurice et al., 2017). Such scenario, however, may not occur if the enrichment of iron in the surface layer is limited as discussed above.

When the most unstable wavelength is longer than 10^4 km, the instability is likely to occur as a global-scale overturn, whereas a wavelength of 10^3 km or shorter may correspond to a dripping-like behavior. As the instability proceeds, the dripping of dense materials is known to form a mushroom-like shape and cause mixing with surrounding materials (e.g., He et al., 1999). Such efficient mixing is also observed in the setting of mantle convection, where upwelling and downwelling plumes entrain ambient materials and mix with them in a growing plume head (e.g., Griffiths & Campbell, 1990). A very short timescale for the Rayleigh-Taylor instability means that a dense layer can start to sink as soon as it is formed, limiting the size of downwelling drips. This suggests that dense materials formed at shallow depth are likely to be mixed well with the underlying layer before it reaches the bottom of the mantle. Even when the viscosity profile with 10% melt is used, a timescale for the instability is likely to be shorter than 1,000 years, so the entire rigid layer may be mixed before the entire magma ocean solidifies. When crystal accumulation, that is, fractional crystallization, is considered, the enrichment of iron in the uppermost layer has been suggested to cause a mantle-wide overturn (Elkins-Tanton et al., 2003), but the instability arising from the superadiabatic thermal structure can start before such large-scale mixing. Similar suggestions have been made previously (Ballmer et al., 2017; Maurice et al., 2017; Boukaré et al., 2018), though the treatment of compositional evolution is more approximate in these studies.

We also conducted the same set of calculations using different a viscosity profile, where a temperature effect is reduced and no viscosity jump is introduced at the 660-km discontinuity. The timescale for the instability becomes longer in this case, but the wavelength of the instability, is still shorter than 1,000 km because of the rapid increase in potential density at the 660-km discontinuity (Figure 8a). As the wavelength of instability is determined by density difference and relative viscosity contrast, dripping-like downwelling is still expected even when an entire viscosity profile is elevated by some factor (e.g., the profile with 10% melt). Therefore, a small-scale instability is likely to homogenize the iron-rich upper mantle and the iron-depleted lower mantle, creating a homogeneous compositional structure, although small-scale heterogeneities may survive. Comparison of Figures 8 and 9 indicates that the time and length scales of instability are very sensitive to an assumed viscosity profile. This significance of viscosity profile for the nature of the Rayleigh-Taylor

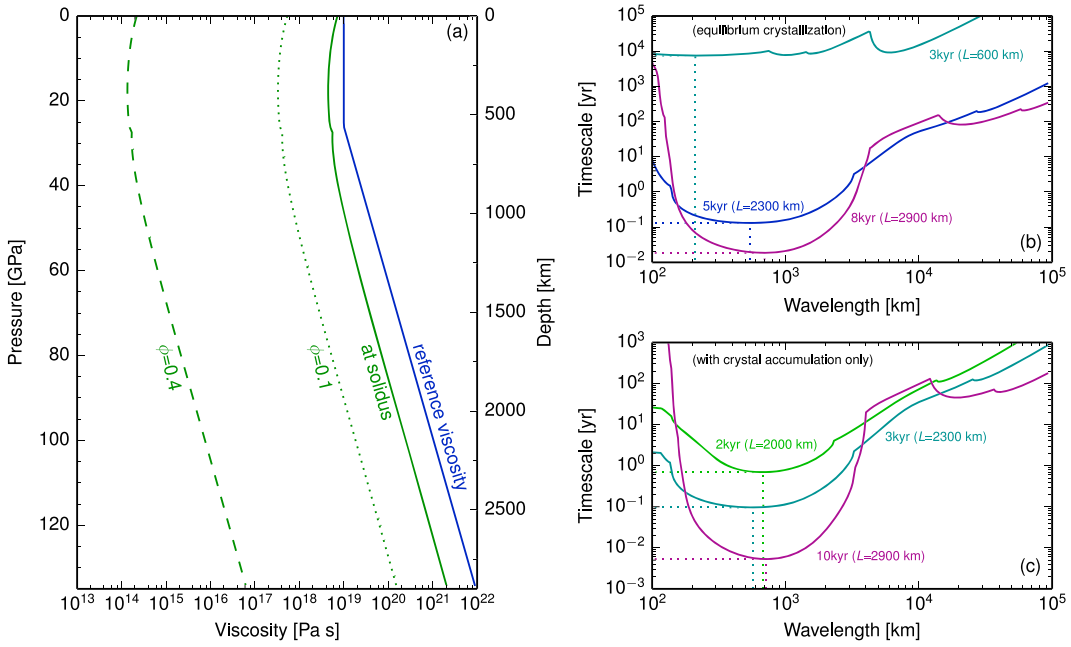

Figure 9. (a) The estimated viscosity profile where no viscosity jump is assumed at the 660-km boundary, and an activation energy of 100 kJ mol^{-1} is used to lower a temperature effect. (b, c) The same with Figure 8, but using a viscosity profile in panel (a) to solve for the propagator matrix method.

instability is not obvious in the previous studies of convective mixing in a solidifying magma ocean (Ballmer et al., 2017; Maurice et al., 2017), in which the treatment of viscosity is kept minimal (e.g., constant viscosity in Ballmer et al. (2017)). The propagator matrix method allows us to evaluate the impact of viscosity as well as other parameters efficiently, though numerical simulation is still important to track the fate of evolving instability.

4.2. Possible Fate of Pure Melt Layers

For the case where only matrix compaction is considered, which occurs when the grain size of solid matrix is larger than 1 cm, a pure melt layer is created above the core-mantle boundary and is enriched in iron, thereby remaining gravitationally stable. Basal magma ocean has often been suggested to result from solidification starting from the midmantle region (e.g., Labrosse et al., 2007; Mosenfelder et al., 2009), but our study shows that it can be created even when solidification starts from the bottom if matrix compaction is efficient. Because the melt originally in the region deeper than 75 GPa is transported to the base of the mantle, incompatible elements originally in this region are likely to be stored in the melt layer without being involved in the mantle convection. Considering that the region below 75 GPa consists of 1/3 of the total mantle, and that 2/3 of melt below 75 GPa is contained basal magma ocean, it can segregate up to 2/9 of total incompatible elements. When volatile elements including water are concentrated in the melt layer, it can further decrease the melting temperature and remain partially molten for a long period of time. Also, such a high-pressure sequestration of incompatible elements could potentially undermine most of the geochemical models for the bulk silicate Earth (Korenaga, 2009), making the thermal budget of Earth geochemically unconstrained.

The further cooling of such basal magma ocean will be slow because it is limited by the convection of the overlying mantle. This may result in sluggish convection, promoting crystal accumulation and thus additional fractionation (Solomatov & Stevenson, 1993b). The remnant of such fractional crystallization is likely to be further enriched in iron, which may have survived until present above the core-mantle boundary. Two-step differentiation process can create two compositionally distinct reservoirs with different degrees of iron enrichment, potentially accounting for the large low shear wave velocity provinces (LLSVP; Garnero & Mcnamara, 2008) and ultralow velocity zones (ULVZs; Williams & Garnero, 1996; Garnero & Lay, 1997), both of which could be explained by the enrichment of iron (e.g., Wicks et al., 2010; Deschamps et al., 2012; Deng et al., 2019). Also, a long-lasting basal magma ocean may affect the pattern of mantle convection as

well (Labrosse et al., 2018). The likelihood of a pure melt layer above the core-mantle boundary thus has significant implications for seismology, geochemistry, and geodynamics.

The pure iron-rich melt layers can emerge at the midmantle region as well (Figures 5b and 6b). For the case with matrix compaction only, the pure melt layer remains lighter than the underlying solidified layer, but the melt layers are predicted to be heavier for the case with both crystal accumulation and matrix compaction (section 3.4). This can trigger the Rayleigh-Taylor instability, which has a shorter timescale compared to the instability of rigid layer (section 4.1). Because the Prandtl number of melt layer is low and the effect of inertia becomes important, the propagator matrix method of Mondal and Korenaga (2018a) cannot be applied. Mondal and Korenaga (2018b) has derived an analytical dispersion relation for a self-gravitating two-layer viscous sphere applicable for any Prandtl number, which shows that the $l = 2$ mode is predicted to be most unstable when the overlying layer has smaller viscosity. They also derived an empirical formula for the corresponding growth rate, σ, as

$$\sigma = 10^{-10.13} r_s^{1.86} (\rho_m - \rho_s)^{1.3} \rho_s^{0.87} (r_m - r_s)^{0.047} \mu_s^{-0.98} \mu_m^{-0.054}, \tag{13}$$

where r_s, ρ_s, and μ_s are the uppermost radius, density, and viscosity of the underlying rigid layer, respectively. The subscript m signifies the properties of the overlying melt layer. When this equation is applied to the pure melt layer at ~50 GPa (Figure 6), the growth rate is likely to be as short as ~10 years, with 10^{18} Pa s for the viscosity of the rigid layer ($\phi = 0.1$ of Figure 7b). Because of the long wavelength of the $l = 2$ mode, most of the melt is likely to directly be transported to the core-mantle boundary, although some degree of mixing is expected to occur with the surrounding mantle by the Kelvin-Helmholtz instability. The pure melt layer is thus expected to result in a basal magma ocean as well.

Depending on the choice of a thermodynamic model, however, the density difference between the melt and underlying solidifying layers may be reversed, keeping the pure melt layer stable at the midmantle depths. When the melt layer is predicted to be lighter than the underlying solidified layer, which is the case for matrix compaction only, such layer is likely to cool gradually, and as in basal magma ocean, further differentiation may occur. When the layer solidifies, however, it becomes heavier than the region below and experiences the Rayleigh-Taylor instability. Therefore, the iron-rich layer is expected to be mixed with the rest of the mantle, leaving small-scale heterogeneities only. Numerical simulation will be necessary to better understand the efficiency of such mixing (Ballmer et al., 2017; Maurice et al., 2017), in which rheological details may play an important role (Manga, 1996).

4.3. The Effect of Surface Temperature on Compositional Structure

The formation of atmosphere is mostly governed by the degassing from magma ocean (e.g., Elkins-Tanton, 2008), and its existence can affect the thermal evolution of magma ocean. During the early stage of evolution, the amount of melt in the system rapidly decreases, which may emit a large amount of greenhouse gases contributing to maintain high temperature at the surface (Lebrun et al., 2013). We tested four different scenarios of solidification, but the rigid layer covers most of the mantle for all four cases within similar time periods, indicating that the release of greenhouse gases from the magma ocean is expected to be similar.

A hotter surface than assumed in our model (i.e., >1500 K) can reduce the magnitude of convective heat flux, slowing down the cooling of magma ocean. A longer timescale, however, does not affect the final thermal and compositional structures for equilibrium crystallization and the case with crystal accumulation only. For crystal accumulation, we assume that the accumulated pile forms instantly, so the cooling rate has no effect, and the structure is rather determined by the thermodynamic properties of the mantle. The mixing by the Rayleigh-Taylor instability remains the same. For the other two cases with matrix compaction, however, longer cooling allows more melt to be extracted by compaction, and therefore a basal magma ocean forms even with smaller grain size. Moreover, higher surface temperature will increase the likelihood of crystal accumulation because, when cooling is slow, the segregation of newly formed grains becomes more efficient, and convective entrainment ineffective.

4.4. Enstatite Chondrite Model for the Earth's Composition

In order to investigate the influence of bulk composition on magma ocean evolution, we have conducted the same set of calculations with an initial composition given by the ternary of MgO: 31.5 wt%, FeO: 14.9 wt%, and SiO_2: 53.6 wt%. This iron- and silicon-rich composition is proposed by Javoy (1995) based on enstatite chondrites, which is isotopically similar to the Earth. Although a more recent study proposes reduced iron

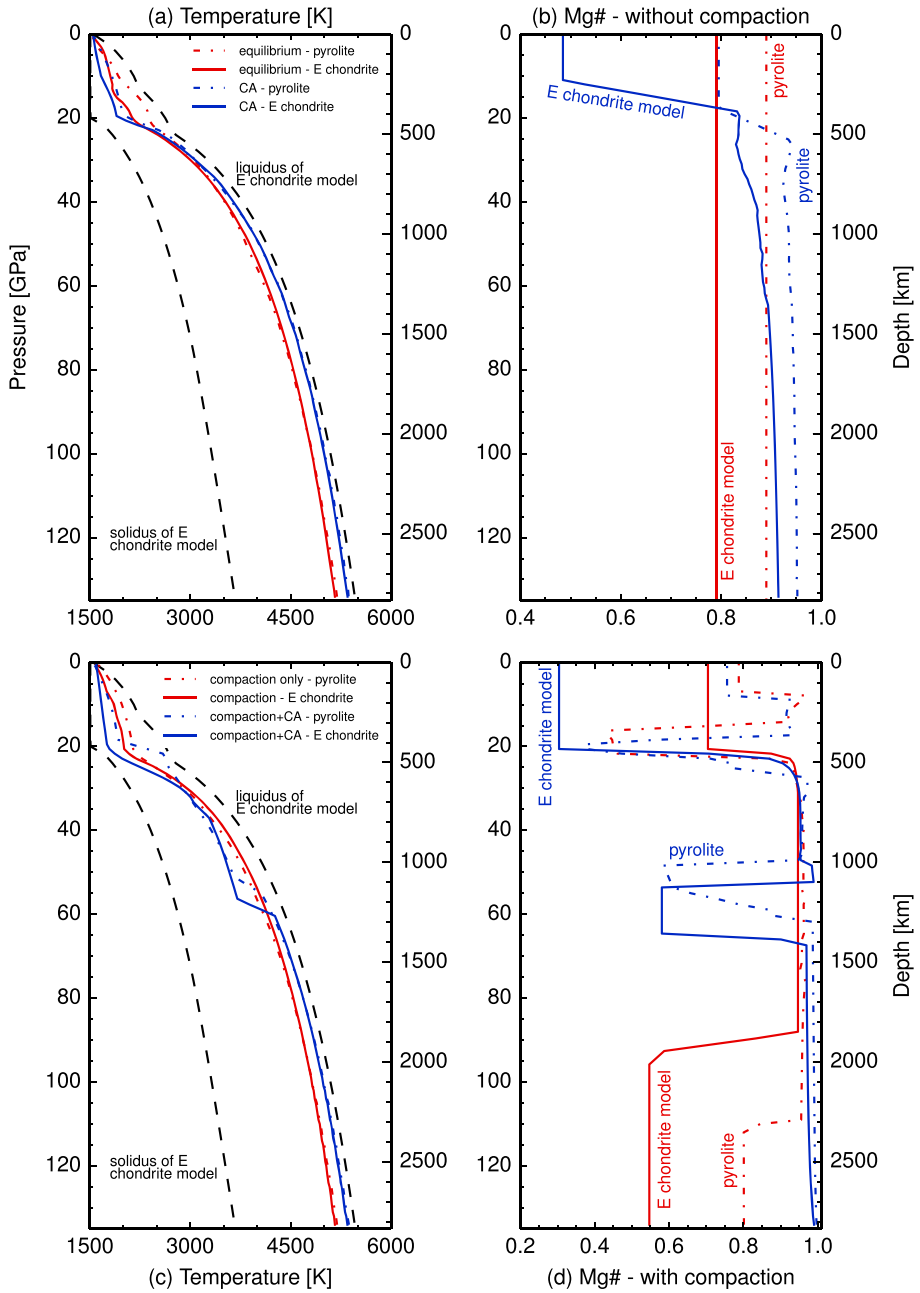

Figure 10. Comparison of (a, c) final thermal and (b, d) compositional structures between the cases where pyrolite (dashed) and the enstatite (E) chondrite model of Javoy (1995) (solid) are used as the initial composition. (a, b) Cases with equilibrium crystallization (red) and with crystal accumulation only (CA; blue). (c, d) Cases with matrix compaction only (red) and with both crystal accumulation and matrix compaction (blue). In (a) and (c), the solidus and liquidus temperatures of the enstatite chondrite model are shown as well (black dashed).

and silicon enrichment (Javoy et al., 2010), the original one is used to provide an estimate for an extreme case. Because of the iron enrichment, the solidus is lower compared to the pyrolitic composition, whereas the liquidus is higher due to high silicon concentration. These two effects cancel out, resulting in a similar 40% melting temperature with the case of pyrolite, and the final thermal structure becomes nearly identical when equilibrium crystallization is considered (Figure 10a). The similarity in the thermal structure holds for the case with crystal accumulation as well, and the enrichment of iron is also seen in the layer near the surface (Figure 10b). The Mg# of the surface layer, however, is substantially lower than the pyrolitic model.

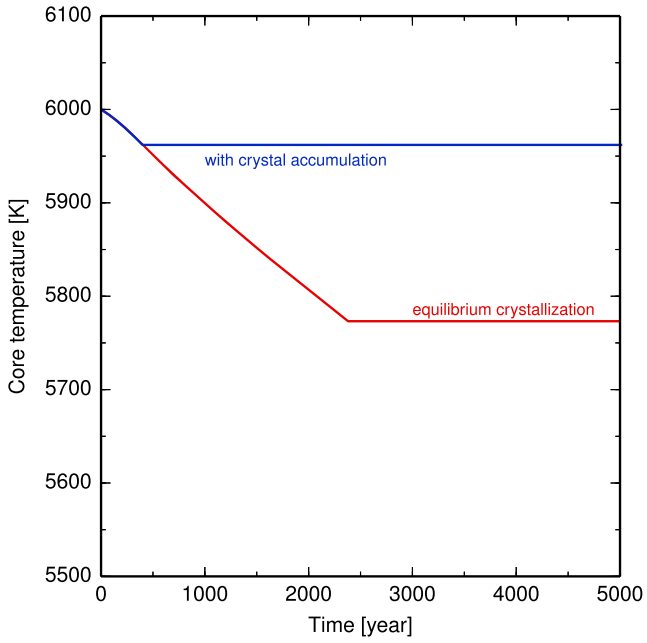

Figure 11. The thermal evolution of the core for the case with equilibrium crystallization (red) and that with crystal accumulation only (blue).

In addition to the low Mg# of the initial composition, the low Fe-Mg partition coefficient creates an Mg-rich rigid layer, and a large amount of iron remains in the surface soft layer. This large compositional contrast, however, decreases the timescale of the Rayleigh-Taylor instability, and such differentiation is thus expected to be eliminated relatively quickly (section 4.1).

The overall characters of the final structure are preserved for the cases with matrix compaction as well. A pure melt layer is formed above the core-mantle boundary for the case with matrix compaction only, and a midmantle melt layer for the case with both matrix compaction and crystal accumulation (Figure 10d). Because the mantle contains more iron, melt becomes heavier than solid matrix for a wider range of pressure, and as a result, the melt layer at the core-mantle boundary becomes thicker. This suggests that more incompatible elements can be stored in this layer.

4.5. Core Cooling

The notable cooling of the core occurs only when the entire mantle is covered by the soft layer. In the cases without crystal accumulation, the core cools by 250 K. When accumulation is considered, on the other hand, the core becomes insulated by the accumulated pile forming at the core-mantle boundary, and the cooling ceases after 500 year, resulting in the temperature drop of only 50 K (Figure 11). This suggests that the core cooling in the magma ocean stage is likely to be insignificant, and an initial core temperature will characterize the thermal state of the core at the beginning of subsolidus convection stage. The core temperature suggested here is similar to that in Andrault et al. (2017), although our result changes with the choice of the initial core temperature.

This insignificant core cooling is in contrast with the modeling results of Monteux et al. (2016), which suggest that the solidification of magma ocean results in a major heat depletion of the core. This difference originates in that their melting model predicts that the rheological transition takes place at a much lower temperature (~4500 K at the core-mantle boundary). In our companion paper, we aimed to construct a thermodynamic model consistent with the currently available high-pressure experiments, but we had to exclude the data on chondritic primitive mantle by Andrault et al. (2011). Based on Gibbs free energy minimization, we are able to calculate melting temperatures of different compositions when a set of thermodynamic parameters is given. Multiple sets of thermodynamic parameters are tested using Monte Carlo sampling to explain existing melting experiments. We were able to constrain the acceptable ranges of thermodynamic parameters that explain a set of melting experiments (e.g., Zerr & Boehler, 1993; Fischer & Campbell, 2010; Fiquet et al., 2010) except for Andrault et al. (2011), which shows lower solidus compared to other studies. Admittedly, high-pressure melting experiments are still highly controversial, and a thermodynamic model constructed based on a larger number of experimental constraints, including partitioning and density measurements, is necessary to resolve the cause of such discrepancy.

5. Conclusion and Outlook

Based on a self-consistent thermodynamic model, we constructed a magma ocean evolution model that is satisfactory in both thermal and compositional aspects. Four end-member scenarios, (1) with no crystal accumulation nor matrix compaction, (2) with crystal accumulation only, (3) with matrix compaction only, and (4) with both crystal accumulation and matrix compaction, are considered, each of which shows different thermal structure and differentiation pattern. The resulting structure, however, may not be gravitationally stable and is subject to the Rayleigh-Taylor instability. The latter three cases are expected to create global-scale compositional stratification with iron-rich and iron-depleted regions, but for the case with crystal accumulation only, such stratification is expected to be quickly homogenized by the instability, and it is unlikely to be maintained as opposed to the other two cases with matrix compaction (Figure 12). The compaction of a crystal-melt mixture is likely to produce pure melt layers, where the melt layers forming at the midmantle region may be gravitationally unstable. These, however, will be transported to the core-mantle boundary without significant mixing with a timescale shorter than 100 years, resulting in a basal magma

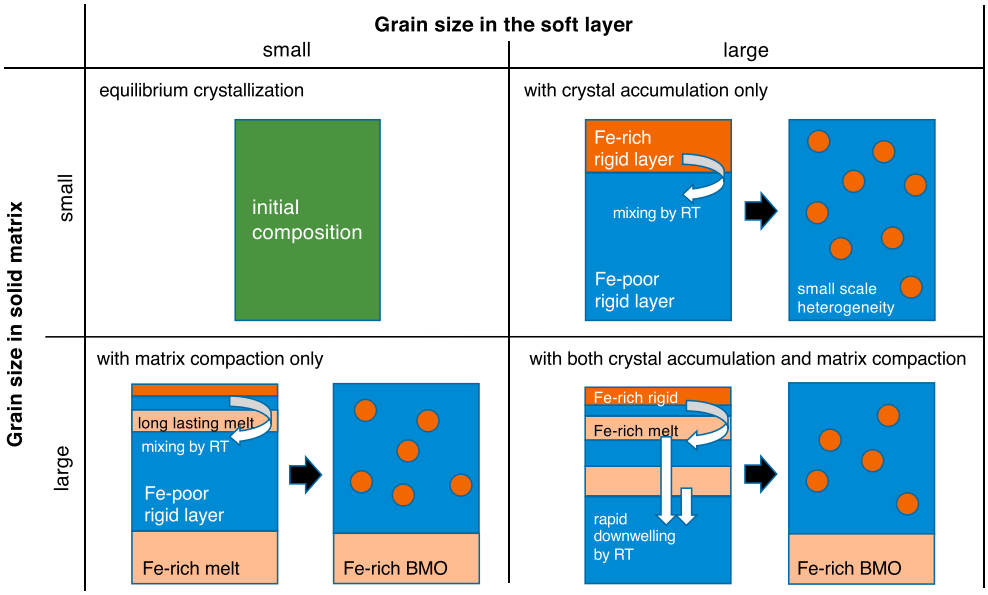

Figure 12. Schematic summary of four cases considered in this study, in terms of final compositional structure. During crystal accumulation and/or matrix compaction, the system experiences global-scale chemical stratification. Such stratification, however, is likely to be eliminated by the Rayleigh-Taylor (RT) instability and results in small-scale chemical heterogeneity for the case with crystal accumulation only. For the cases with matrix compaction, Fe-rich pure melt layers (light orange) are created in the midmantle region, which will be rapidly transported downward by the $l = 2$ mode of the Rayleigh-Taylor instability. Some degree of mixing may occur during the downwelling, but most of the melt is expected to sink to the core-mantle boundary, forming a long-lasting basal magma ocean (BMO). With our choice of model parameters, a grain size of 1 mm in solid matrix corresponds to the cases with small grain size, and that of 1 cm to large grain size.

ocean. An iron-rich melt layer is created above the core-mantle boundary also for the case with matrix compaction only.

Because both grain size and the viscosity of the rigid layer are uncertain, it is hard to determine the most probable scenario. The compositional structure after the Rayleigh-Taylor instability, however, is expected to be mostly homogeneous for the case with crystal accumulation only, although small-scale heterogeneities may persist. The efficiency of mixing by the Rayleigh-Taylor instability will control the likely size of chemical heterogeneities at the start of subsolidus mantle convection. Crystal accumulation at the bottom and the following overturn of the entire mantle have been proposed to create an iron-rich layer at the core-mantle boundary, but the cases with matrix compaction are more likely to exhibit such a feature. Regardless of grain size in the soft layer, an iron-rich melt layer at the base of the mantle is formed when grain size in the solid matrix is large enough. Even with a smaller grain size, the compaction of matrix can produce a basal magma ocean when the timescale for cooling is long enough.

This study focused on placing bounds on compositional differentiation, but it turns out that matrix compaction and the Rayleigh-Taylor instability can occur on a similar timescale. As opposed to rapid mixing expected from our analysis of the Rayleigh-Taylor instability, recent numerical studies suggest that mixing timescale can be longer than the age of planets (Maurice et al., 2017; Boukaré et al., 2018). This discrepancy likely originates in differences in temperature and viscosity profiles assumed for the rigid layer. A final thermal structure is determined by a thermodynamic model, and the thermal structure affects the viscosity profile. Therefore, obtaining a more reliable thermodynamic model is essential to better understand the evolution after the rheological transition.

The improvement of a thermodynamic model continues to be an important task as more results from high-pressure experiments become available. The partition coefficient of iron between melt and solid phase plays an important role in determining the thickness of the melt layer above the core-mantle boundary, yet the experimental results are still controversial (Nomura et al., 2011; Andrault et al., 2012; Tateno et al., 2014). Other elements including Al, Ca, and Ti may affect the partitioning coefficient, and incorporating these ele-

ments into the model will be desirable. Despite the paucity of relevant data, the effect of water must play a crucial role in the melting and degassing of magma ocean (e.g., Elkins-Tanton, 2008; Lebrun et al., 2013; Andrault et al., 2014; Hier-Majumder & Hirschmann, 2017), which is important not only for solidification, but also for the formation of atmosphere and oceans (e.g., Elkins-Tanton, 2011; Hamano et al., 2013; Salvador et al., 2017). There is thus a clear demand for a more comprehensive thermodynamic model including the effects of volatile elements.

Acknowledgments
This work was sponsored by the National Science Foundation under grant EAR-1753916. This work was also supported in part by the facilities and staff of the Yale University Faculty of Arts and Sciences High Performance Computing Center. The authors thank two anonymous reviewers and the Associate Editor for constructive comments and suggestions, which helped to improve the clarity of the manuscript. Thermodynamic data for solid components are taken from the paper of Stixrude and Lithgow-Bertelloni (2011), and those for liquid components are from our companion paper (Miyazaki & Korenaga, 2019).

References

Abe, Y. (1993). Thermal evolution and chemical differentiation of the terrestrial magma ocean. *Geophysical Monograph*, *74*, 41–54.

Abe, Y. (1997). Thermal and chemical evolution of the terrestrial magma ocean. *Physics of the Earth and Planetary Interiors*, *100*, 27–39. https://doi.org/10.1016/S0031-9201(96)03229-3

Abe, Y., & Matsui, T. (1988). Evolution of an impact-generated H_2O-CO_2 atmosphere and formation of a hot proto-ocean on Earth. *Journal of the Atmospheric Sciences*, *45*, 3081–3101. https://doi.org/10.1175/1520-0469(1988)045<3081:EOAIGH>2.0.CO;2

Andrault, D., Bolfan-Casanova, N., Bouhifd, M. A., Boujibar, A., Garbarino, G., & Manthilake, G. (2017). Toward a coherent model for the melting behavior of the deep Earth's mantle. *Physics of the Earth and Planetary Interiors*, *265*, 67–81. https://doi.org/10.1016/j.pepi.2017.02.009

Andrault, D., Bolfan-Casanova, N., Lo Nigro, G., Bouhifd, M. A., Garbarino, G., & Mezouar, M. (2011). Solidus and liquidus profiles of chondritic mantle: Implication for melting of the Earth across its history. *Earth and Planetary Science Letters*, *304*, 251–259. https://doi.org/10.1016/j.epsl.2011.02.006

Andrault, D., Pesce, G., Bouhifd, M. A., Bolfan-Casanova, N., Henot, J.-M., & Mezouar, M. (2014). Melting of subducted basalt at the core-mantle boundary. *Science*, *344*, 892–895. https://doi.org/10.1126/science.1250466

Andrault, D., Petitgirard, S., Lo Nigro, G., Devidal, J. L., Veronesi, G., Garbarino, G., & Mezouar, M. (2012). Solid-liquid iron partitioning in Earth's deep mantle. *Nature*, *487*, 354–357. https://doi.org/10.1038/nature11294

Ballmer, M. D., Lourenço, D. L., Hirose, K., Caracas, R., & Nomura, R. (2017). Reconciling magma-ocean crystallization models with the present-day structure of the Earth's mantle. *Geochemistry, Geophysics, Geosystems*, *18*, 2785–2806. https://doi.org/10.1002/2017GC006917

Boukaré, C.-E., Parmentier, E. M., & Parman, S. W. (2018). Timing of mantle overturn during magma ocean solidification. *Earth and Planetary Science Letters*, *491*, 216–225. https://doi.org/10.1016/j.epsl.2018.03.037

Boukaré, C.-E., Ricard, Y., & Fiquet, G. (2015). Thermodynamics of the MgO-FeO-SiO_2 system up to 140 GPa: Application to the crystallization of Earth's magma ocean. *Journal of Geophysical Research: Solid Earth*, *120*, 6085–6101. https://doi.org/10.1002/2015JB011929

Braithwaite, J., & Stixrude, L. (2019). Melting of $CaSiO_3$ perovskite at high pressure. *Geophysical Research Letters*, *46*, 2037–2044. https://doi.org/10.1029/2018GL081805

Brown, S. M., Elkins-Tanton, L. T., & Walker, R. J. (2014). Effects of magma ocean crystallization and overturn on the development of ^{142}Nd and ^{182}W isotopic heterogeneities in the primordial mantle. *Earth and Planetary Science Letters*, *408*, 319–330. https://doi.org/10.1016/j.epsl.2014.10.025

Buening, D. K., & Buseck, P. R. (1973). Fe-Mg lattice diffusion in olivine. *Journal of Geophysical Research*, *78*, 6852–6862.

Buffett, B. A., Huppert, H. E., Lister, J. R., & Woods, A. W. (1996). On the thermal evolution of the Earth's core. *Journal of Geophysical Research*, *101*, 7989–8006.

Campbell, G. A., & Forgacs, G. (1990). Viscosity of concentrated suspensions: An approach based on percolation theory. *Physical Review A*, *41*, 4570–4573.

Canup, R. M. (2008). Accretion of the Earth. *Philosophical Transactions of the Royal Society A*, *366*, 4061–4075. https://doi.org/10.1098/rsta.2008.0101

Deng, J., & Lee, K. K. M. (2017). Viscosity jump in the lower mantle inferred from melting curves of ferropericlase. *Nature Communications*, *8*, 1997. https://doi.org/10.1038/s41467-017-02263-z

Deng, J., Miyazaki, Y., & Lee, K. K. M. (2019). Implications for the melting phase relations in the MgO-FeO system at core-mantle boundary conditions. *Journal of Geophysical Research: Solid Earth*, *124*. https://doi.org/10.1029/2018JB015499

Deschamps, F., Cobden, L., & Tackley, P. J. (2012). The primitive nature of large low shear-wave velocity provinces. *Earth and Planetary Science Letters*, *350*, 198–208. https://doi.org/10.1016/j.epsl.2012.07.012

Dingwell, D. B., Courtial, P., Giordano, D., & Nichols, A. R. (2004). Viscosity of peridotite liquid. *Earth and Planetary Science Letters*, *226*, 127–138. https://doi.org/10.1016/j.epsl.2004.07.017

Du, Z., & Lee, K. K. M. (2014). High-pressure melting of MgO from (Mg,Fe)O solid solutions. *Geophysical Research Letters*, *3*, 8061–8066. https://doi.org/10.1002/2014GL061954.Received

Dullien, F. A. L. (1992). *Porous media: Fluid transport and pore structure* (2nd ed.). San Diego: Academic Press.

Elkins-Tanton, L. T. (2008). Linked magma ocean solidification and atmospheric growth for Earth and Mars. *Earth and Planetary Science Letters*, *271*, 181–191. https://doi.org/10.1016/j.epsl.2008.03.062

Elkins-Tanton, L. T. (2011). Formation of early water oceans on rocky planets. *Astrophysics and Space Science*, *332*, 359–364. https://doi.org/10.1007/s10509-010-0535-3

Elkins-Tanton, L. T. (2012). Magma oceans in the inner solar system. *Annual Review of Earth and Planetary Sciences*, *40*, 113–139. https://doi.org/10.1146/annurev-earth-042711-105503

Elkins-Tanton, L. T., Parmentier, E. M., & Hess, P. C. (2003). Magma ocean fractional crystallization and cumulate overturn in terrestrial planets: Implications for Mars. *Meteoritics and Planetary Science*, *38*, 1753–1771. https://doi.org/10.1111/j.1945-5100.2003.tb00013.x

Fiquet, G., Auzende, A. L., Siebert, J., Corgne, A., Bureau, H., Ozawa, H., & Garbarino, G. (2010). Melting of peridotite to 140 gigapascals. *Science*, *329*, 1516–1518. https://doi.org/10.1126/science.1192448

Fischer, R. A., & Campbell, A. J. (2010). High-pressure melting of wüstite. *American Mineralogist*, *95*, 1473–1477. https://doi.org/10.2138/am.2010.3463

Foley, B. J., Bercovici, D., & Elkins-Tanton, L. T. (2014). Initiation of plate tectonics from post-magma ocean thermochemical convection. *Journal of Geophysical Research: Solid Earth*, *119*, 8538–8561. https://doi.org/10.1002/2014JB011121

Garnero, E. J., & Lay, T. (1997). Lateral variations in lowermost mantle shear wave anisotropy beneath the north Pacific and Alaska. *Journal of Geophysical Research*, *102*, 8121–8135.
Garnero, E. J., & Mcnamara, A. K. (2008). Structure and dynamics of Earth's lower mantle. *Science*, *320*, 626–629.
Griffiths, R. W., & Campbell, I. H. (1990). Stirring and structure in mantle starting plumes. *Earth and Planetary Science Letters*, *99*, 66–78.
Hamano, K., Abe, Y., & Genda, H. (2013). Emergence of two types of terrestrial planet on solidification of magma ocean. *Nature*, *497*, 607–610. https://doi.org/10.1038/nature12163
He, X., Zhang, R., Chen, S., & Doolen, G. D. (1999). On the three-dimensional Rayleigh-Taylor instability. *Physics of Fluids*, *11*, 1143–1152. https://doi.org/10.1063/1.869984
Hier-Majumder, S., & Hirschmann, M. M. (2017). The origin of volatiles in the Earth's mantle. *Geochemistry, Geophysics, Geosystems*, *18*, 3078–3092. https://doi.org/10.1002/2017GC006937
Javoy, M. (1995). The integral enstatite chondrite model of the Earth. *Geophysical Research Letters*, *22*, 2219–2222. https://doi.org/10.1029/95GL02015
Javoy, M., Kaminski, E., Guyot, F., Andrault, D., Sanloup, C., Moreira, M., et al. (2010). The chemical composition of the Earth: Enstatite chondrite models. *Earth and Planetary Science Letters*, *293*, 259–268. https://doi.org/10.1016/j.epsl.2010.02.033
Karato, S.-i., & Wu, P. (1993). Rheology of the upper mantle: A synthesis. *Science*, *260*, 771–778.
Korenaga, J. (2009). A method to estimate the composition of the bulk silicate Earth in the presence of a hidden geochemical reservoir. *Geochimica et Cosmochimica Acta*, *73*, 6952–6964. https://doi.org/10.1016/j.gca.2009.08.020
Korenaga, J. (2013). Initiation and evolution of plate tectonics on Earth: Theories and observations. *Annual Review of Earth and Planetary Sciences*, *41*, 117–151. https://doi.org/10.1146/annurev-earth-050212-124208
Labrosse, S., Hernlund, J. W., & Coltice, N. (2007). A crystallizing dense magma ocean at the base of the Earth's mantle. *Nature*, *450*, 866–869. https://doi.org/10.1038/nature06355
Labrosse, S., Morison, A., Deguen, R., & Alboussiere, T. (2018). Rayleigh-Bénard convection in a creeping solid with melting and freezing at either or both its horizontal boundaries. *Journal of Fluid Mechanics*, *846*, 5–36. https://doi.org/10.1017/jfm.2018.258
Lebrun, T., Massol, H., Chassefière, E., Davaille, A., Marcq, E., Sarda, P., et al. (2013). Thermal evolution of an early magma ocean in interaction with the atmosphere. *Journal of Geophysical Research: Planets*, *118*, 1155–1176. https://doi.org/10.1002/jgre.20068
Lesher, C. E., & Spera, F. J. (2015). Thermodynamic and transport properties of silicate melts and magma. In H. Sigurdsson, C. E. Lesher, & F. J. Spera (Eds.), *The Encyclopedia of Volcanoes* (pp. 113–141). Amsterdam: Elsevier Inc. https://doi.org/10.1016/B978-0-12-385938-9.00005-5
Liebske, C., Schmickler, B., Terasaki, H., Poe, B. T., Suzuki, A., Funakoshi, K.-i., et al. (2005). Viscosity of peridotite liquid up to 13 GPa: Implications for magma ocean viscosities. *Earth and Planetary Science Letters*, *240*, 589–604. https://doi.org/10.1016/j.epsl.2005.10.004
Lyubetskaya, T., & Korenaga, J. (2007). Chemical composition of Earth's primitive mantle and its variance: 1. Method and results. *Journal of Geophysical Research*, *112*, B03211. https://doi.org/10.1029/2005JB004223
Manga (1996). Mixing of heterogeneities in the mantle: Effect of viscosity differences. *Geophysical Research Letter*, *23*, 403–406.
Martin, D., & Nokes, R. (1989). A fluid-dynamical study of crystal settling in convecting magmas. *Journal of Petrology*, *30*, 1471–1500. https://doi.org/10.1093/petrology/30.6.1471
Matsui, T., & Abe, Y. (1986). Evolution of an impact-induced atmosphere and magma ocean on the accreting Earth. *Nature*, *319*, 303–305.
Maurice, M., Tosi, N., Samuel, H., Plesa, A.-C., Huttig, C., & Breuer, D. (2017). Onset of solid-state mantle convection and mixing during magma ocean solidification. *Journal of Geophysical Research: Planets*, *122*, 577–598. https://doi.org/10.1002/2016JE005250
McDonough, W. F., & Sun, S.-s. (1995). The composition of the Earth. *Chemical Geology*, *120*, 223–253. https://doi.org/10.1016/0012-821X(95)00123-T
Mei, S., Bai, W., Hiraga, T., & Kohlstedt, D. L. (2002). Influence of melt on the creep behavior of olivine-basalt aggregates under hydrous conditions. *Earth and Planetary Science Letters*, *201*, 491–507. https://doi.org/10.1016/S0012-821X(02)00745-8
Miyazaki, Y., & Korenaga, J. (2017). Effects of chemistry on vertical dust motion in early protoplanetary disks. *The Astrophysical Journal*, *849*, 41. https://doi.org/10.3847/1538-4357/aa8cd1
Miyazaki, Y., & Korenaga, J. (2019). On the timescale of magma ocean solidification and its chemical consequences: 1. Thermodynamic database for liquid at high pressures. *Journal of Geophysical Research: Solid Earth*, *124*, 3382–3398. https://doi.org/10.1029/2018JB016932
Mondal, P., & Korenaga, J. (2018a). A propagator matrix method for the Rayleigh-Taylor instability of multiple layers: A case study on crustal delamination in the early Earth. *Geophysical Journal International*, *212*, 1890–1901. https://doi.org/10.1093/gji/ggx513
Mondal, P., & Korenaga, J. (2018b). The Rayleigh-Taylor instability in a self-gravitating two-layer viscous sphere. *Geophysical Journal International*, *212*, 1859–1867. https://doi.org/10.1093/gji/ggx507
Monteux, J., Andrault, D., & Samuel, H. (2016). On the cooling of a deep terrestrial magma ocean. *Earth and Planetary Science Letters*, *448*, 140–149. https://doi.org/10.1016/j.epsl.2016.05.010
Mosenfelder, J. L., Asimow, P. D., Frost, D. J., Rubie, D. C., & Ahrens, T. J. (2009). The $MgSiO_3$ system at high pressure: Thermodynamic properties of perovskite, postperovskite, and melt from global inversion of shock and static compression data. *Journal of Geophysical Research*, *114*, B01203. https://doi.org/10.1029/2008JB005900
Mukhopadhyay, S. (2012). Early differentiation and volatile accretion recorded in deep-mantle neon and xenon. *Nature*, *486*, 101–104. https://doi.org/10.1038/nature11141
Nakajima, M., & Stevenson, D. J. (2015). Melting and mixing states of the Earth's mantle after the Moon-forming impact. *Earth and Planetary Science Letters*, *427*, 286–295. https://doi.org/10.1016/j.epsl.2015.06.023
Nomura, R., Ozawa, H., Tateno, S., Hirose, K., Hernlund, J., Muto, S., et al. (2011). Spin crossover and iron-rich silicate melt in the Earth's deep mantle. *Nature*, *473*, 199–202. https://doi.org/10.1038/nature09940
Reese, C. C., & Solomatov, V. S. (2006). Fluid dynamics of local Martian magma oceans. *Icarus*, *184*, 102–120. https://doi.org/10.1016/j.icarus.2006.04.008
Salvador, A., Massol, H., Davaille, A., Marcq, E., Sarda, P., & Chassefière, E. (2017). The relative influence of H_2O and CO_2 on the primitive surface conditions and evolution of rocky planets. *Journal of Geophysical Research: Planets*, *122*, 1458–1486. https://doi.org/10.1002/2017JE005286
Siggia, E. D. (1994). High Rayleigh number convection. *Annual Review of Fluid Mechanics*, *26*, 137–168. https://doi.org/10.1146/annurev.fluid.26.1.137
Solomatov, V. (2015). Magma oceans and primordial mantle differentiation (2nd ed.). In V. Solomatov (Ed.), *Treatise on Geophysics* (Vol. 9, pp. 81–104). Amsterdam, The Netherlands: Elsevier. https://doi.org/10.1016/B978-044452748-6.00141-3
Solomatov, V. S., Olson, P., & Stevenson, D. J. (1993). Entrainment from a bed of particles by thermal convection. *Earth and Planetary Science Letters*, *120*, 387–393. https://doi.org/10.1016/0012-821X(93)90252-5

Solomatov, V. S., & Stevenson, D. J. (1993a). Nonfractional crystallization of a terrestrial magma ocean. *Journal of Geophysical Research*, *98*, 5391–5406.

Solomatov, V. S., & Stevenson, D. J. (1993b). Suspension in convective layers and style of differentiation of a terrestrial magma ocean. *Journal of Geophysical Research*, *98*, 5375–5390.

Solomatov, V. S., & Stevenson, D. J. (1993c). Kinetics of crystal growth in a terrestrial magma ocean. *Journal of Geophysical Research*, *98*, 5407–5418.

Stevenson, D. J., Spohn, T., & Schubert, G. (1983). Magnetism and thermal evolution of the terrestrial planets. *Icarus*, *54*, 466–489. https://doi.org/10.1016/0019-1035(83)90241-5

Stixrude, L., & Lithgow-Bertelloni, C. (2011). Thermodynamics of mantle minerals—II. Phase equilibria. *Geophysical Journal International*, *184*, 1180–1213. https://doi.org/10.1111/j.1365-246X.2010.04890.x

Tateno, S., Hirose, K., & Ohishi, Y. (2014). Melting experiments on peridotite to lowermost mantle conditions. *Journal of Geophysical Research: Solid Earth*, *119*, 4684–4694. https://doi.org/10.1002/2013JB010616.Received

Turcotte, D. L., & Schubert, G. (2002). *Geodynamics* (2nd ed.). New York, NY: Cambridge University Press.

Wicks, J. K., Jackson, J. M., & Sturhahn, W. (2010). Very low sound velocities in iron-rich (Mg,Fe)O: Implications for the core-mantle boundary region. *Geophysical Research Letters*, *37*, L15304. https://doi.org/10.1029/2010GL043689

Williams, Q., & Garnero, E. J. (1996). Seismic evidence for partial melt at the base of Earth's mantle. *Science*, *273*, 1528–1530.

Zerr, A., & Boehler, R. (1993). Melting of (Mg, Fe)SiO_3-perovskite to 625 kilobars: Indication of a high melting temperature in the lower mantle. *Science*, *262*, 553–555.